Article

Accessing Near-Field Strong Ground Motions Using a Multi-Scheme Method in the Kalawenguquan Fault, Xinjiang, China

Jiangyi Li [1],*, Bengang Zhou [1], Zhongtai He [1], Haomin Ji [1], Lei Wang [1,2] and Guodong Bao [1]

[1] Key Laboratory of Seismic and Volcanic Hazards, Institute of Geology, China Earthquake Administration, Beijing 100029, China; zhoubg@ies.ac.cn (B.Z.)
[2] Shandong Earthquake Agency, Jinan 250014, China
* Correspondence: lijiangyi@ies.ac.cn

Abstract: The middle segment of the Kalawenguquan fault has been active since the Holocene, with a maximum credible earthquake magnitude of M_S 7.5. We established two source models based on empirical relationships, as well as geological, geomorphological, and seismic characteristics. Taking into account the uncertainties of simulation parameters, we adopted the stochastic finite-fault method to calculate all combinations of a multi-scheme simulation. The effects of different source models, initial rupture points, and site locations on the prediction of ground motion parameters were analyzed. The results indicate that when a site is located on a smaller asperity and is a certain distance from the largest asperity, the simulation results are higher. For different sites, when the initial rupture point is located near the smaller rather than the larger asperity, the acceleration response spectra are higher. Our results show that the relationships between the initial rupture points, asperities, and sites have a significant impact on the simulation results. Therefore, our study highlights the relevance of determining the initial rupture point and source model to obtain a reasonable evaluation for near-field strong ground motion simulations at major infrastructures.

Keywords: ground motion simulation; stochastic finite-fault method; maximum credible earthquake; asperity; logic tree

1. Introduction

Strong ground motions induced by devastating large earthquakes will not only cause many casualties but also destroy human habitats and threaten the safety of major infrastructures [1,2]. Thus, many countries have developed seismic codes to guide the earthquake-resistant design of various building structures [3–6]. In particular, seismic hazard assessment of the engineering sites of major infrastructures is required since it is of great importance to the sustainable development of critical infrastructures such as nuclear power plants, reservoirs, and hydropower stations, especially for those located in seismically active regions.

Deterministic seismic hazard analysis considers worst-case scenarios or the maximum credible earthquake to estimate the intensity of seismic ground motion distributions. The current approach to obtaining deterministic ground motion parameters is to employ only one set of modeling parameters for ground motion simulations or calculate average values by using ground motion prediction equations. However, it is difficult to obtain accurate ground motion simulation parameters, and ground motion prediction equations from both domestic and foreign sources lack near-field strong ground motion recordings [7–12]. The reasonable evaluation of near-field ground motion parameters offers important engineering significance for seismic fortification, which has an effect on the evaluation of structural responses and the results of nonlinear analysis [13–16]. Regionally adoptable ground motion simulation parameters are critical for obtaining reasonable simulation results.

However, aleatory and epistemic uncertainties inevitably exist when determining these parameters; therefore, different researchers can obtain different ground motion simulation parameters for the same fault [17,18]. Therefore, it is particularly important to consider the uncertainties of modeling parameters when calculating peak ground acceleration (PGA) and the response spectra of near-field large earthquakes when using ground motion simulations, considerations often overlooked in simulation work [19,20].

Over the past two decades, the stochastic finite-fault method has been applied to the simulation of near-field ground motion parameters of large earthquakes, providing reliable ground motion predictions for areas that lack strong ground motion records [21–29]. This method can be used to effectively synthesize Fourier amplitude spectra, response spectra, and the time history of acceleration [30]. This method can also be used to analyze the effect of modeling parameter uncertainty on ground motion simulations [19,20]. Yu et al. [19] analyzed the applicability of the stochastic finite-fault method in near-field large earthquake simulations. Based on the parameters of uncertainty analysis, they established a comprehensive evaluation system for ground motion parameters and considered the influence of different seismogenic tectonics on a dam site. Zhang et al. [20] used the stochastic finite-fault method to consider the impact of the source, propagation path, and site conditions. They analyzed fault size, rupture velocity, shear wave velocity, stress drop, kappa value, and Q value and produced a corresponding range of values. In this study, based on a multi-scheme simulation and the stochastic finite-fault method, we focused on analyzing the impact of different source models, initial rupture points, and site locations on the simulation of near-field large earthquakes.

The Tianshan orogenic belt is a compressive orogenic belt located within the Eurasian continent (Figure 1a). It is the result of the collision of the Indian and Eurasian plates during the Late Cenozoic [31,32]. Previous geological and geodesy studies have shown that the northern and southern boundary fault zones of the Tianshan Mountains exhibit strong structural deformation [33–36]. The Tianshan Mountains are one of the most active seismic regions on the Chinese mainland, as testified by the occurrence of 15 earthquakes of $M \geq 7$ leading to surface rupture. As an internal block of the Tianshan region, the Yultuz Basin is surrounded by multiple active late Quaternary faults, which were associated with the 2012 Xinyuan–Hejing M_S 6.6 earthquake and the 1944 Xinyuan $M\,7\frac{1}{4}$ earthquake. The Kalawenguquan fault is known to be the northern edge of the Nalati fault and controls the northwestern edge of the Yultuz Basin. It is about 400 km long, spanning 360 km in Xinjiang, China, and about 40 km in Kazakhstan (Figure 1b). This left-lateral strike-slip fault has an average strike of N64°E and dips 60–80° to the south [37]. Previous studies characterized Kalawenguquan fault activity using geological and geomorphological features such as alluvial fans, river terraces, and gullies [38,39]. Using remote sensing multi-source data, such as Gaofen-2 images, Landsat 8 satellite images, and aerial high-resolution images, Chen [37] evaluated the geometry and seismic hazard posed by the Kalawenguquan fault. However, geometric structure, sliding rate, and fault activity of the Kalawenguquan fault have not yet been comprehensively understood. Wang et al. [40] conducted systematic research on the middle segment (F1–3 in Figure 1b) of the Kalawenguquan fault using high-resolution remote sensing image interpretation, geological field surveys, geomorphological surveys, drone aerial surveys, trench excavation, and the dating of trench samples with the radiocarbon-14 dating method. The results indicated that the F1-3 segment of the Kalawenguquan fault has been an active fault since the Holocene. Furthermore, the Kalawenguquan fault was the seismogenic structure of the 2007 M_S 5.9 Tekesi earthquake, but its accumulated energy was not fully released [41]. There is still a possibility of large earthquakes occurring on this fault in the future.

Due to abundant water resources, infrastructures such as reservoirs, tunnels, pipelines, and other facilities have been planned to be built in the Kalawenguquan region. The Kalawenguquan fault is about 43 km away from Tekesi City and 60 km away from Zhaosu City, and it crosses the Yining–Akesu Railway. Therefore, reasonable evaluations of ground motion parameters for near-field large earthquakes have important engineering significance

for the seismic safety of major infrastructures and transportation routes and for the urban seismic planning of cities in Tekesi and Zhaosu. In the current study, we designed a multi-scheme simulation and used the stochastic finite-fault method to consider the uncertainty of various modeling parameters for the F1-3 fault.
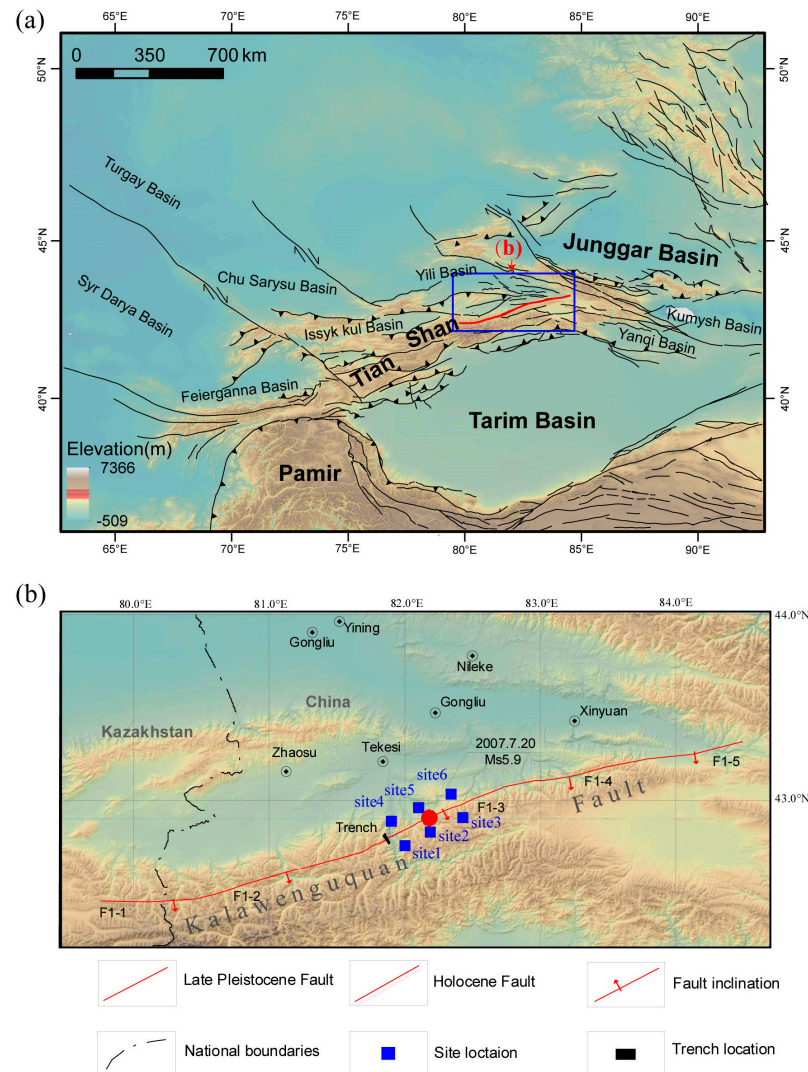
Figure 1. (**a**) Tectonic map of the Tianshan orogenic belt. The blue square indicates the location of the Kalawenguquan fault. (**b**) Close-up view of the Kalawenguquan fault segments. The red line, blue squares, and black rectangle represent the fault surface, site locations, and trench location, respectively.

2. Materials and Methods

2.1. Materials

2.1.1. Maximum Credible Earthquake Magnitude

According to the differences in the seismic and geological activity of the Kalawenguquan fault, it can be divided into five segments (see Figure 1b).

Wang et al. [40] determined the horizontal displacement of the F1-3 segment to be 3.4 m. Based on a large number of historical earthquake source rupture models, Wells and Coppersmith [42] established the following empirical relationship between the maximum displacement and moment magnitude for strike-slip faults:

$$Mw = 6.81 + 0.68 \log D, \ \sigma = 0.29 \tag{1}$$

Cheng et al. [43] compiled a homogeneous M_W-based historical earthquake catalog based on three Chinese earthquake catalogs and three global M_W catalogs. They regressed a constrained M_S–M_W relationship and their regression errors when $M_S \geq 7.0$ for the period from 1976 to 2015 as follows:

$$M_W = (1.28 \pm 0.20)M_S - (2.42 \pm 1.47), \ \sigma = 0.14 \tag{2}$$

Thus, we used Equations (1) and (2) to determine that the maximum credible earthquake for the F1-3 segment was M_S 7.5.

2.1.2. Dip Angle

The F1-3 segment of the Kalawenguquan fault is the seismogenic fault responsible for the Tekesi M_S 5.9 earthquake that occurred on 20 July 2007 [41]. The focal mechanism solution for this earthquake showed that the dip angle of the fault rupture plane was almost vertical. Wang et al. [40] excavated a trench (Figure 1b) perpendicular to the fault's scarps that showed that the nearly vertical F1-3 fault dips toward southeast (145°) with a dip angle of 85°. Thus, for the multi-scheme method, we set the fault dip angles to 80°, 85°, and 90°, which were equally weighted.

2.1.3. Rupture Length and Width

Based on Equation (2), we converted the maximum credible earthquake magnitude (M_S 7.5) of the F1-3 fault to M_W 7.18. Considering the regression uncertainties in the magnitude conversion relationship and the characteristics of the fault activity, we added the calculated mean of M_W 7.18 with one standard deviation (0.14) to obtain a maximum potential earthquake magnitude of M_W 7.3. Wells and Coppersmith [42] established an empirical relationship between the surface rupture length and width for strike-slip faults and moment magnitude; it is shown below:

$$Mw = 5.16 + 1.12 \log L, \ \sigma = 0.28 \tag{3}$$

$$Mw = 3.80 + 2.59 \times \log(W), \ \sigma = 0.45 \tag{4}$$

We used Equations (3) and (4) to determine that the length of the fault rupture surface caused by M_W 7.3 earthquakes occurring on the F1-3 fault was about 82 km, and the width of the rupture surface was about 22 km.

2.1.4. Quality Factor

Based on digital seismograms recorded at 17 stations in Xinjiang, Tang and Li [44] used a genetic algorithm and the method proposed by Atkinson and Mereu [45] to calculate the inelastic attenuation coefficient of seismic waves. The frequency-dependent S-wave Q in the Xinjiang region was estimated to correspond to $Q = 460.7f^{0.515}$. Using the same inverted method, Liu and Li [46] estimated the relationship between the Q values of inelastic attenuation in northern Tianshan and determined that $Q = 465.2f^{0.53}$, which is similar to the result obtained in [44]. Zhao et al. [47] used different inversion methods to invert the frequency-dependent $Q(f)$ models for 13 regions and the site responses of 348 stations for about 2573 events of $3.0 \leq M_L \leq 6.0$ from 2001 to 2010. The quality factor in the central and eastern parts of the Tianshan Mountains was $Q(f) = 460.7f^{0.52}$. To demonstrate the influence of different $Q(f)$ models, we calculated their acceleration response spectra using one source model, an initial rupture point of 1, and a rupture distance of 10 km, as shown in Figure 2. We found that the quality factor had a relatively small impact on the ground motion simulation results. Therefore, considering the seismic data and the different study areas referred to above, we adopted the quality factor of $Q(f) = 460.7f^{0.52}$ obtained by [47] as the only model value for our multi-scheme simulations.
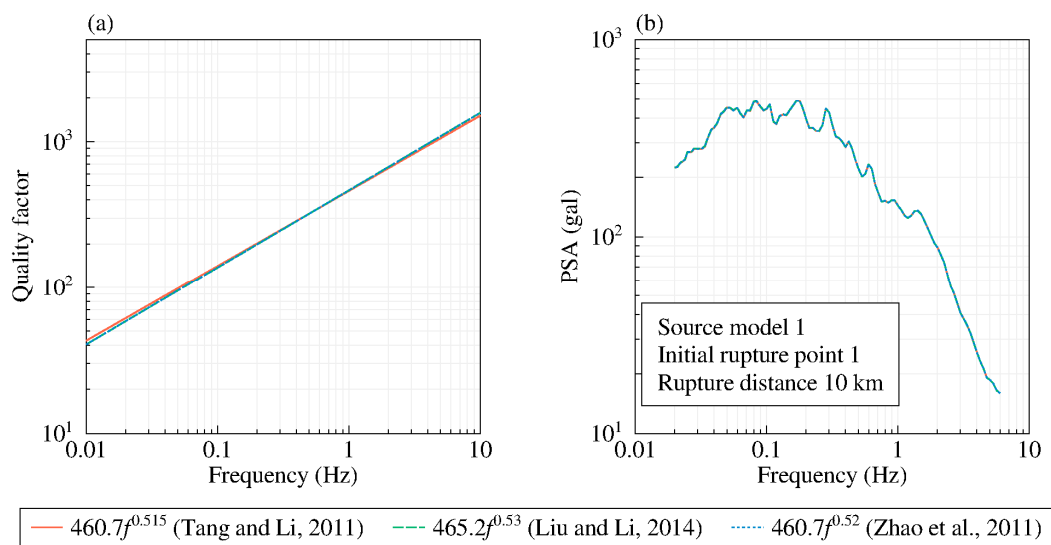
Figure 2. Comparison of (**a**) the selected quality factor models and (**b**) the simulation results using the selected quality factor models for a given simulated earthquake scenario [44,46,47].

2.1.5. Stress Drop

Using seismic data recorded during 112 earthquakes ($3.0 \leq M_S \leq 7.3$), Xia [48] determined the stress drop value of the Yutian area to be 8.2–118 bar. Before the Yutian M_S 7.3 earthquake and one hour after it, the stress drop was around 10 bars. Liu et al. [46] used the omega-squared model to obtain the source parameters of 161 earthquakes ($2.5 \leq M_L \leq 5.0$) that occurred between 2009 and 2011, and the obtained stress drop was 0–60 bar with an average value of 30 bar. Therefore, the stress drop values selected as the two schemes for the ground motion simulations were 30 and 60 bar, which were equally weighted.

2.1.6. High-Frequency Attenuation

In the stochastic finite-fault method, the total site effect is accounted for by the production of a crustal amplification function and a high-frequency attenuation function. Atkinson and Silva [49] analyzed seismic data from Eastern Canada and found that the high-frequency attenuation κ_0 was influenced by site conditions. Even bedrock sites exhibited significant high-frequency attenuation, although the effect was not significant, with values ranging from 0.02 to 0.04 s. Campbell [50] estimated the κ_0 for National Earthquake Hazard Reduction Program (NEHRP) BC site profiles (sediment plus hard rock) in the Mississippi embayment and the Atlantic coastal plain. Their results showed that the κ_0 values increased from about 0.009 to 0.031 s for a sediment thicknesses ranging from 116 to 600 m. Fu and Li [51] used a database of 1597 accelerograms from more than 500 events recorded at 44 stations in the range of 0–300 km ($3.3 < M_S < 8.0$) from the 2008 Wenchuan and 2013 Lushan earthquakes to study the characteristics of κ. The κ_0 values of the JYD, LSJ, and TQD site class A stations were 0.0034, 0.0022, and 0.0027 s, respectively. A total of 334 accelerograms of 42 small-to-moderate earthquakes recorded at 36 strong-motion stations were used to investigate the ground motion characteristics of the southwestern margin of the Sichuan–Yunnan rhombic block [52]. The calculated κ_0 values of the three site class A stations ranged from 0.0014 to 0.0028 s. There are almost no research results regarding κ_0 for our study area, so we chose the empirical κ_0 value mentioned above for hard bedrock sites because major infrastructure sites are generally built on bedrock. Thus, we adopted κ_0 values of 0.015, 0.025, and 0.035 s by considering the uncertainty with equal weighting in the multi-scheme method.

2.1.7. Site Amplification Factor

Based on the arrival time data for $M_S \geq 1.5$ earthquakes recorded between 2009 and 2020 by the permanent stations of the Xinjiang regional digital seismic network, emergency mobile stations, and some broadband seismic stations, Liu et al. [53] examined the high-resolution three-dimensional P-wave and S-wave velocity structures of the crust and uppermost mantle in the study area, along with hypocentral relocations, using the double-difference tomography method. We adopted their one-dimensional S-wave velocity structure of the shallow and deep crust in the middle of the Tianshan Mountains near the F1-3 fault segment (Table 1). We calculated the average crustal amplification factor of the rock site by using the quarter-wavelength approximation method [54], as shown in Figure 3.

Table 1. The velocity structure.

Depth/km	Vp/(km/s)	Vs/(km/s)
0.0	5.11	3.06
5.0	5.46	3.40
10.0	6.04	3.51
15.0	6.03	3.56
20.0	6.07	3.67
25.0	6.22	3.56
30.0	6.22	3.68
40.0	6.67	3.69
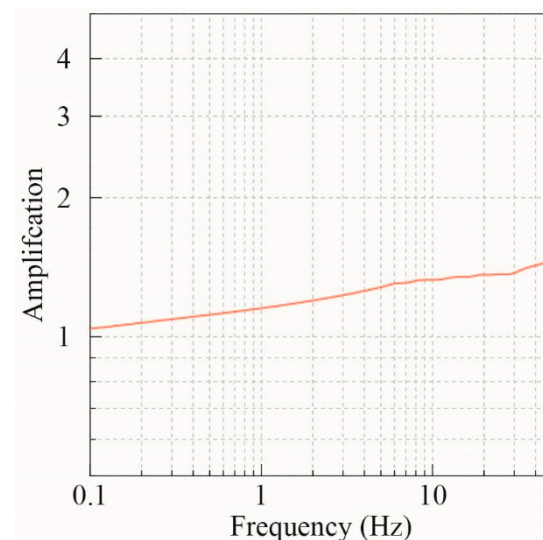
Figure 3. Average crustal amplification factor of the rock site in the study area.

2.2. Source Model

The uncertainty of specifying appropriate methods for characterizing the source characteristics of future earthquakes is one of the main uncertainties in the prediction of strong ground motion. It is challenging to predict the source rupture process before an earthquake occurs, and even the source models of different earthquakes that occur in the same seismogenic fault may differ, as is the case for the 2008 Wenchuan M_W 7.9 earthquake and the 2013 Lushan M_W 6.7 earthquake on the Longmen Shan fault. Therefore, determining how to provide appropriate source slip models on fault zones for the prediction of near-field strong ground motion for major infrastructure projects is a key issue that needs to be addressed.

We established two slip models to consider the source uncertainties. Slip Model 1 is based on empirical models, and Slip Model 2 is based on seismic and geological characteristics. We defined an asperity as a rectangular region that facilitates the generation of slip models for future earthquakes [55]. Based on slip models of 15 earthquakes worldwide,

Somerville et al. [55] conducted a statistical analysis of the empirical relationships of asperities. Their results showed that the 15 earthquakes analyzed had 39 asperities, or an average of 2.6 asperities each. Since the maximum credible earthquake magnitude of the F1-3 fault is M_W 7.3 and the corresponding fault rupture length is 82 km, we set two asperities for the source model scheme, as introduced in detail below.

2.2.1. Slip Model 1

Somerville et al.'s [55] result showed that the combined area of asperities, A_{as}, on average occupies 22% of the total rupture area, which can be shown as follows:

$$A_{as} = 0.22 \times L \times W \tag{5}$$

Here, L and W are the rupture length and rupture width, respectively.

The area of the largest asperity, A_{a1}, is approximately 16% of the total rupture area, and the area of the other asperity, A_{a2}, is 6% of the total rupture area:

$$A_{a1} = 0.16 \times L \times W \tag{6}$$

$$A_{a2} = 0.06 \times L \times W \tag{7}$$

We assigned the asperities and other rupture areas different slips to appropriately represent the inhomogeneity of the stress and slip on the rupture area. The average slip of rupture area $\bar{D}$ was calculated as follows [56]:

$$\bar{D} = \frac{M_0}{\mu A} \tag{8}$$

where $\mu = 3 \times 10^{11} \text{dyne/cm}^2$ is the average shear modulus of the crust, A is the rupture area, and M_0 is the seismic moment. The seismic moment can be calculated based on the empirical relationship between the moment magnitude of the maximum credible earthquake and the seismic moment [57]:

$$M_W = \frac{2}{3} \log M_0 - 10.7 \tag{9}$$

The ratio of the average slip on the asperities to the average slip over the whole rupture plane is independent of seismic moment, and the average value for the events studied was about 2 [55]. Thus, the average slip on the asperities, D_{as}, and on the other rupture areas, D_{bk}, can be calculated as follows:

$$D_{as} = 2.0 \times \bar{D} \tag{10}$$

$$D_{bk} = 0.71 \times \bar{D} \tag{11}$$

Based on the slip distribution data from 13 earthquakes [55] and additional data from 16 earthquakes, Wang [58] studied the characteristic parameters of asperities for shallow earthquakes. For a strike-slip fault, the semi-empirical relationship between the distance X_{as} from the fault reference point to the center of the largest asperity along the strike direction and the rupture length is as follows:

$$\log X_{as} = \log L - 0.30 \tag{12}$$

The semi-empirical relationship between the distance Y_{as} from the top depth of a fault to the center of the largest asperity along the dip direction and the rupture width is as follows:

$$\log Y_{as} = \log W - 0.28 \tag{13}$$

The empirical relationship between the length of the largest asperity, L_{as}, and the fault rupture length is as follows:

$$\log L_{as} = \log L - 0.66 \tag{14}$$

The empirical relationship between the width of the largest asperity, W_{as}, and the fault rupture width is as follows:

$$\log W_{as} = \log W - 0.23 \tag{15}$$

Referring to these empirical relationships, we determined the size and center location of the largest asperity on the fault rupture surface, which was in the middle of the F1-3 fault. In addition, another smaller asperity was set at the location closest to Site 1, which was tested to obtain the same results as setting it near Site 3, as shown in Figure 1b. Slip model 1, determined based on the empirical relationships, is shown in Figure 4a. The determined parameters are listed in Table 2.
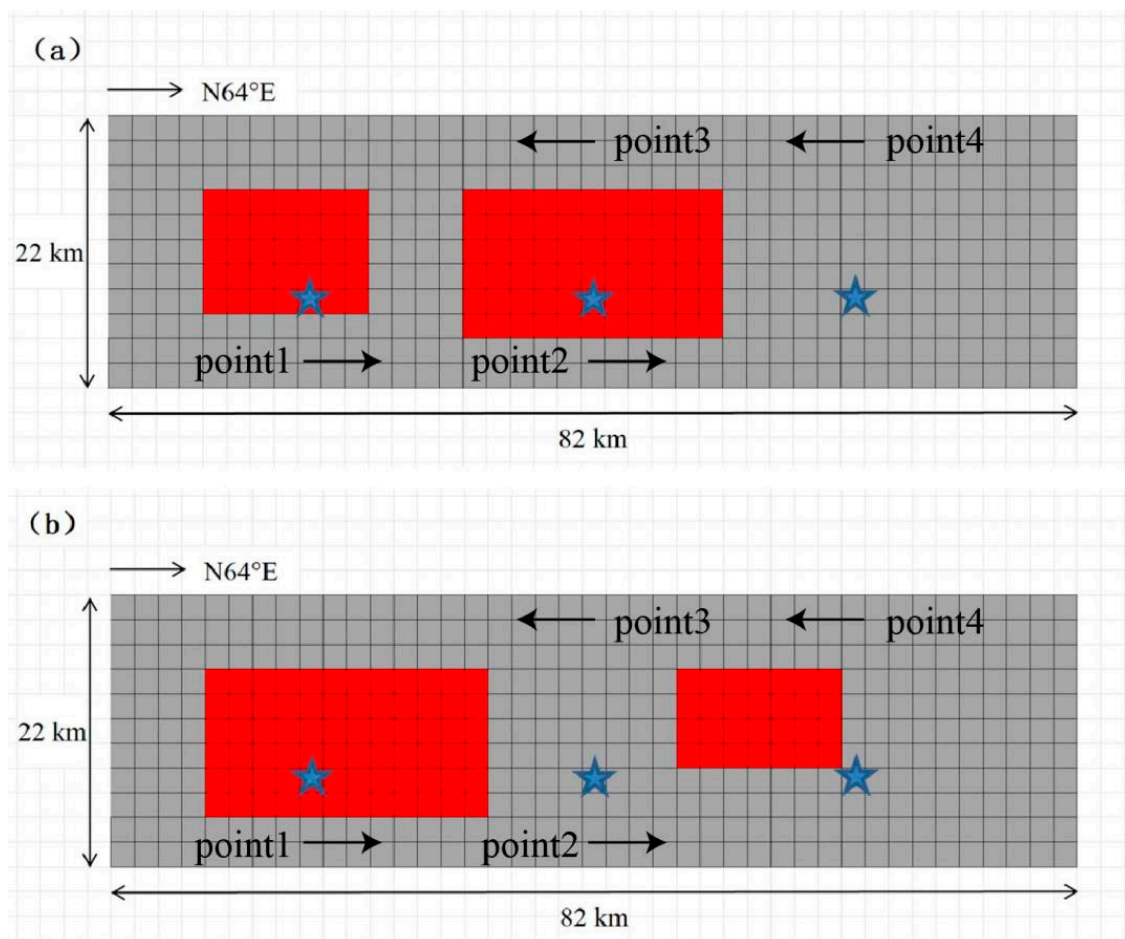
Figure 4. Schematic diagram of the source model. (**a**) Source Model 1, established from empirical relationships, and (**b**) Source Model 2. The red areas represent the asperities, the gray areas represent the other rupture area of the F1-3 fault, the blue stars represent the initial rupture points, and the arrows show different rupture schemes; the subfault size is 2 × 2 km.

Table 2. Parameters used for the stochastic finite-fault method.

Parameter	Value	Parameter	Value
Fault strike	N64°E	Average slip of rupture area (m)	1.85
Inclination	Southeast	Slip of asperity (m)	3.7
Fault dip angle (°)	80, 85, 90	Slip of background (m)	1.29
Fault rupture length (km)	82	Depth from upper fault boundary (km)	0
Fault rupture width (km)	22	S-wave velocity (km/s)	3.6
Fault rupture area (km^2)	1804	Average crustal density (g/cm^3)	2.8
Moment magnitude	7.3	Stress drop (bar)	30.0, 60.0
Seismic moment	1.0×10^{20} N · m	Geometrical spreading	$1/R$
dl (km)	2	Quality factor	$Q(f) = 460.7 \, f^{0.52}$
dw (km)	2	κ_0 (s)	0.015, 0.025, 0.035
Maximum asperity area (km^2) (Slip Model 1)	288	Other asperity area (km^2) (Slip Model 1)	112
Maximum asperity area (km^2) (Slip Model 2)	264	Other asperity area (km^2) (Slip Model 2)	140

2.2.2. Slip Model 2

The scaling relationships of earthquake rupture models are based on a relatively small set of events, and there must be uncertainty in establishing a source model based on empirical relationships. Therefore, we needed to identify an asperity on a rupture plane to overcome our inability to accurately predict slip models of future earthquakes. Determining earthquake recurrences, fault slip accumulation patterns, and offset accumulation patterns based on geomorphic evidence can assist in identifying asperities. To determine its fault activity characteristics, Wang et al. [40] conducted geological field and geomorphological surveys of the F1-3 segment. They found a series of relatively intact linear reverse fault scarps and large earthquake surface fractures along the length of the fault. A digital elevation model image clearly showed offsets along the F1-3 fault, including visibly sinistral offset rivers and gullies and T2 terraces. Therefore, it could be reasonably estimated that the target fault was active in the recent period. They also excavated a trench, whose location is shown in Figure 1b. They determined that four events had occurred on the F1-3 fault that had offset sediments deposited during the Holocene. The radiocarbon-14 dating results for the trench samples indicated that the elapsed time of the latest event was approximately 1670 a, which is close to the characteristic earthquake recurrence interval of 2000 a [40]. The geological and geomorphological results presented in [40] revealed that the southwestern segment of the F1-3 fault is the most active, and there is a high seismic risk of large earthquakes on this fault in the future. Therefore, we set the largest asperity to be in this location.

On 20 July 2007, the Xinjiang Tekesi M_S 5.9 earthquake occurred in the eastern part of the F1-3 fault (see Figure 1b). Based on the tectonic stress field and the focal mechanism solution of the Tekesi M_S 5.9 earthquake, Li et al. [41] ascertained that the NEE-trending Kalawenguquan fault was the seismogenic structure for this earthquake, specifically where the fault is inclined toward the southeast with a dip angle greater than 50°. There is an earthquake gap near the source, which may be due to the relatively complete medium in this area. The F1-3 fault exhibits strong tectonic activity with high stress accumulation [59]. The absence of $M_S > 4.0$ aftershocks in the Tekesi earthquake sequence may indicate that the energy accumulated in the F1-3 fault has not been fully released, and there is a risk of strong earthquakes in the future.

In summary, accounting for the geological, geomorphological, and seismic characteristics of the F1-3 fault, we established Slip Model 2. We set the largest asperity to be near Site 1 (see Figure 1b) and the smallest asperity to be at the epicenter of the 2007 Tekesi M_S 5.9 earthquake. The location of the asperities and initial rupture points in the fault rupture area are shown in Figure 4b.

2.3. Stochastic Finite-Fault Modeling Methods

To evaluate the ground motion parameters generated by a maximum credible earthquake at a near-field site, we employed stochastic finite-fault modeling based on dynamic corner frequency, which has been confirmed to be suitable for engineering applications [60] (EXSIM12). In the stochastic finite-fault modeling of ground motions, a rupture fault is divided into N subfaults with a length of Δl and a width of Δw, where each subfault is considered a small point source. The ground motion contributed by each subfault can be calculated using the stochastic point-source method and then summed at the observation point with an appropriate time delay to obtain the acceleration time series, a(t), caused by the entire ruptured fault, as follows:

$$a(t) = \sum_{i=1}^{nl} \sum_{j=1}^{nw} a_{ij}\left(t + \Delta t_{ij}\right) \tag{16}$$

where *nl* is the number of subfaults along the strike of the entire ruptured fault and *nw* is the number of subfaults along the dip. Δt_{ij} denotes the relative delay time for the radiated wave from the *ij*th subfault to the site. $a_{ij}(t)$ represents the acceleration time series of the *ij*th subfault at the site simulated using the stochastic point-source method [30].

Motazedian and Atkinson [60] reported the dynamic corner frequency and acceleration spectrum of the shear wave of the *ij*th subfault *Aij*(*f*) as follows:

$$A_{ij}(f) = \left\{ CM_{0ij}\,(2\pi f)^2 / \left[1 + \left(f_{0ij}\right)^2\right] \right\} \left\{ G\left(R_{ij}\right) \exp\left(-\pi f R_{ij}/Q\beta\right) \right\} \left\{ A(f) \exp\left(-\pi f \kappa_0\right) \right\} \tag{17}$$

where M_{0ij}, f_{0ij}, and R_{ij} represent the seismic moment of the subfault, the dynamic corner frequency, and the distance from the *ij*th subfault to the site, respectively. For the constant $C = \frac{R^{\theta\varphi}FV}{4\pi\rho\beta^3}$, $R^{\theta\varphi}$ denotes the radiation pattern (average value of 0.55 for shear waves); *F* denotes the free surface amplification, which is usually taken as 2.0; the partition of the two horizontal components of *V* is 0.71; ρ denotes the density near the source; and β denotes the average crustal shear wave velocity [61,62]. The term $\exp(-\pi f \kappa_0)$ is a high-cut filter that considers the near-surface attenuation effects, and κ_0 denotes the spectral decay at high frequencies [51,63]. The quality factor $Q(f)$ is related to the anelastic attenuation caused by the propagation path. $G(R_{ij})$ is the geometrical spreading, which is given by a trilinear piecewise model, and $A(f)$ is the local site amplification, as mentioned in Boore's work [62].

The source corner frequency of the *ij*th subfault is expressed as follows:

$$f_{0ij} = 4.9 \times 10^{+6} \cdot \beta \left(\Delta\sigma / M_{0ij}\right)^{1/3} \tag{18}$$

where $\Delta\sigma$ is the stress drop and M_{0ij} represents the seismic moment of the *ij*th subfault, which can be expressed as follows:

$$M_{0ij} = \frac{M_0}{N} \frac{S_{ij}}{\sum_{l=1}^{nl}\left(\sum_{k=1}^{nw} S_{kl}\right)/N} = \frac{M_0 S_{ij}}{\sum_{l=1}^{nl} \sum_{k=1}^{nw} S_{kl}} \tag{19}$$

Here, S_{ij} is the relative slip weight of the *ij*th subfault.

The dynamic corner frequency of the *ij*th subfault, $f_{0ij}(t)$, can be defined as a function of $N_R(t)$ and the cumulative number of ruptured subfaults at time *t* as follows:

$$f_{0ij}(t) = 4.9E^{+6} \cdot N_R(t)^{-1/3} \cdot \beta \left(\Delta\sigma / M_{0\text{ave}}\right)^{1/3} \tag{20}$$

where $M_{0\text{ave}} = \frac{M_0}{N}$ represents the average seismic moment of all subfaults. Moreover, Motazedian and Atkinson [60] introduced a scaling factor, H_{ij}, that conserves the high-frequency spectral level of subfaults, which can be expressed as follows:

$$H_{ij} = \left\{ \frac{N \int f^2 / \left[1 + (f/f_0)^2\right] df}{\int f^2 / \left[1 + (f/f_{0ij})^2\right] df} \right\}^{1/2} \tag{21}$$

Thus, the acceleration spectrum of the *ij*th subfault, $A_{ij}(f)$, is expressed as follows:

$$A_{ij}(f) = C M_{0ij} H_{ij} (2\pi f)^2 / \left[1 + (f/f_{0ij})^2\right] \tag{22}$$

Boore [64] introduced a modification of Frankel's filter to constrain the low-frequency source spectrum of this method, as follows:

$$S(f) = C \frac{1 + (f/f_{0sf})^2}{1 + (f/f_{0eff})^2} \tag{23}$$

where f_{0sf} represents the corner frequency of the *ij*th subfault, $C = \sqrt{N}/H$, and $f_{0eff} = f_{0sf}/\sqrt{C}$ represents the effective source corner frequency for the *ij*th subfaults.

2.4. Multi-Scheme Ground Motion Simulations

The current approach to predict ground motion parameters at near-field sites is usually to take only one set of ground motion simulation parameters or to use the ground motion prediction equation to calculate average values, thereby ignoring inevitable aleatory and epistemic uncertainties. Thus, we used different modeling parameters to design a logic tree for ground motion simulation. As mentioned above, taking the F1-3 fault as the seismogenic structure, we determined multiple values for the fault's geometric parameters, slip models, and other ground motion modeling parameters. We then designed multi-scheme simulations with different parameter combinations and calculated the results of each scheme using the stochastic finite-fault method. The stochastic finite-fault modeling method contains aleatory uncertainties. Thus, to make the simulation results more reliable and the standard deviation of the average response spectrum more stable, we conducted 30 simulations for each group of the above parameters, with a weight coefficient of 1/30 for each scheme. A flowchart of the multi-scheme ground motion simulation for the 2160 schemes is shown in Figure 5. The fault geometric parameters and ground motion modeling parameters used in our study are shown in Table 2.
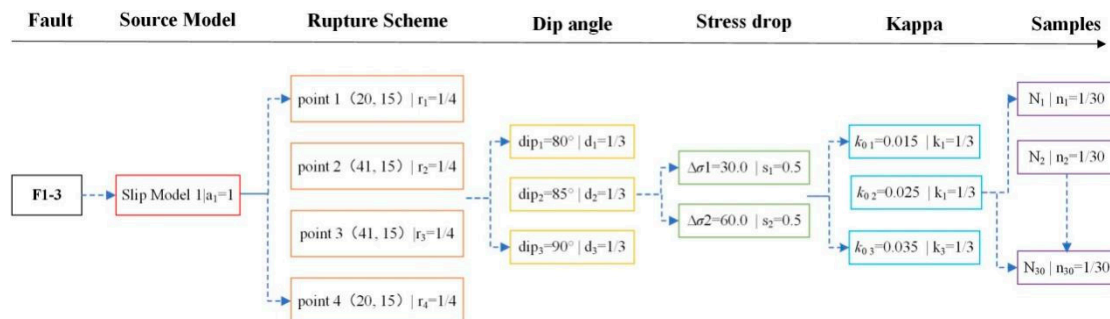
Figure 5. Multi-scheme flowchart. Slip Model 1, point$_i$, dip$_i$, $\Delta\sigma_i$, $\kappa_{0\ i}$, and N$_i$ denote the source model, location of the initial rupture point, dip angle, stress drop, kappa, and number of simulations, respectively, and a$_1$, r$_i$, d$_i$, s$_i$, k$_i$, and n$_i$ denote the corresponding weight coefficients, respectively. For the rupture schemes, the values in parentheses represent the distances between the initial rupture point and the fault reference points along the fault strike and rupture width, respectively.

The formula for the total weight coefficient W_i of the *i*th scheme is as follows:

$$W_i = a_i \cdot r_i \cdot d_i \cdot s_i \cdot k_i \cdot n_i \cdot \tag{24}$$

where a_i, r_i, d_i, s_i, k_i, and n_i represent the weights of the slip model, initial rupture point, dip angle, stress drop, κ_0, and number of simulations, respectively, of the *i*th scheme.

## 3. Results

3.1. The Influence of Slip Models

In addition to Slip Models 1 and 2, we used a random model for a comparative analysis [60]. Based on the modeling parameters and their weights, as shown in Figure 5, we selected Site 1 to calculate the ground motion parameters for the different slip models. The calculated PGA and acceleration response spectra for each scheme were statistically analyzed. The minimum, average, maximum, and 50th-, 84th-, and 95th-percentile PGA values for the three source models are listed in Table 3. Figure 6 shows the average and the 84th-percentile statistical acceleration spectra for all schemes of each slip model.

Table 3. Peak ground acceleration (PGA) simulation results for Site 1.

Source Model	PGA (gal)					
	Min	50th-Percentile	Average	84th-Percentile	95th-Percentile	Max
Slip Model 1	145.5	349.7	348.5	512.9	622.8	929.1
Slip Model 2	100.2	239.2	238.5	350.0	423.4	687.3
Random model	88.6	236.0	236.8	350.4	428.5	667.1
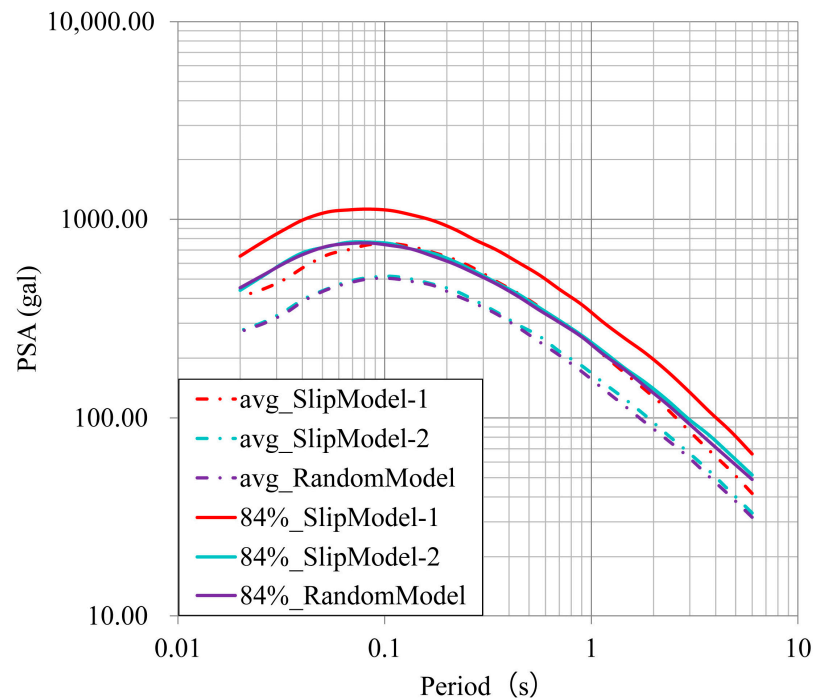
Figure 6. Acceleration response spectra of the different source models.

As shown in Table 3, the minimum, average, maximum, and 50th-, 84th-, and 95th-percentile PGA values for Slip Model 1 are significantly higher than those for Slip Model 2 and the random model. The minimum, average, and 50th-percentile PGA values for Slip Model 2 are higher than those for the random model and lower than those for the random model for the 84th- and 95th-percentiles. Though the maximum PGA for Slip Model 2 is higher than that for the random model, we consider it an accidental occurrence of a single event or a value caused by a random slip distribution model and thus not representative of the overall characteristics.

In Figure 6, the acceleration response spectra of the average and 84th-percentile values of Slip Model 1 are higher than those of Slip Model 2 and the random model, while the results of Slip Model 2 are comparable to those of the random model and are close to the average response spectra of Slip Model 1. The difference between the results of Slip Model 1 and Slip Model 2 is significant, while the difference between Slip Model 2 and the random model is relatively small. When T < 1 s, the 84th-percentile acceleration value of Slip Model 2 is close to the result of the random model, and the 84th-percentile acceleration of Slip Model 2 is higher after T > 1 s. The patterns of the average value for these two slip models are similar. When T < 0.1 s, the average values of Slip Model 2 and the random model are comparable, and the result of Slip Model 2 is higher after T > 0.1 s.

Because the values and weights of each modeling parameter were the same, we considered the differences in the results to be caused by the different slip models used for the rupture area. By analyzing the slip distribution characteristics of the different slip models, we found that the PGA and acceleration response spectra of the random model were similar to those of Slip Model 2, in which the largest asperity was closer to the site, but significantly different from those of Slip Model 1, in which the largest asperity was further from the site. Therefore, we could conclude that the random model may not be applicable for the prediction of near-field ground motion parameters for large earthquakes, which requires the consideration of special situations.

3.2. The Influence of Initial Rupture Points

The location of the initial rupture point controls the distribution and superposition of energy on the rupture plane [62]. In this study, three initial rupture points were established on the fault, namely, points a quarter of the way in from both ends of the fault and a point in the middle of the fault, as shown in Figure 4. The depth of the three rupture points was set to 15 km. Different rupture propagation directions may result in different ground motion parameters. In this case, the rupture direction could be from either the southwest end of the fault to the northeast end of the fault or vice versa. Thus, combining the rupture directions and the initial rupture points, we adopted four rupture schemes, represented by points 1–4 in Figure 4. Moreover, adopting different weight coefficients can also lead to different results. We designed 12 weight schemes with different weight coefficient combinations for points 1–4, as shown in Table 4.

Table 4. Weight schemes for the different initial rupture points.

Weight Scheme	Point 1	Point 2	Point 3	Point 4
1	0.1	0.4	0.4	0.1
2	0.2	0.3	0.3	0.2
3	0.4	0.1	0.1	0.4
4	0.4	0.1	0.4	0.1
5	0.3	0.2	0.2	0.3
6	0.3	0.2	0.3	0.2
7	0.2	0.2	0.3	0.3
8	0.1	0.1	0.4	0.4
9	0.4	0.4	0.1	0.1
10	0.3	0.3	0.2	0.2
11	0.1	0.4	0.1	0.4
12	0.25	0.25	0.25	0.25

Based on the values and weights of the other simulation parameters shown in Figure 5, we adopted Site 1 in Figure 1b and the stochastic finite-fault approach to obtain the simulation results. Comparisons of the 84th-percentile PGA and acceleration response spectra of the ground motion simulations for Slip Models 1 and 2 are presented in Tables S1 and S2, respectively. The results show that the different weight schemes of the initial rupture point had a very limited impact on the simulation result for both Slip Models 1 and 2. Detailed analysis revealed that the simulation results for Slip Models 1 and 2 show slight differences

when T < 0.5 s, but these results are almost equal when T > 0.5 s. For Slip Model 1, the PGAs for weight schemes 1, 4, and 9 are slightly higher than those for the other weight schemes. We found that the total weights of points 1–3 located near the asperities for weight schemes 1, 4, and 9 are higher. Conversely, the PGAs of weight schemes 3, 8, and 11 are lower, and their weight compositions show that the weights of points 1–3 are lower, while the weights of point 4 are higher. For Slip Model 2, the simulation results are slightly higher when the sum weights of points 2 and 3 are higher, as reflected by the simulation results of weight scheme 1. In summary, the different weight schemes of the initial rupture point had a very limited impact on the simulation results.

Then, with the other parameters remaining unchanged, we adopted weight scheme 12 to analyze the impact of different initial rupture point depths along the rupture width on the simulation results. We calculated the average and 84th-percentile acceleration response spectra of the ground motion simulations for the two source models using the following depths for the initial rupture point: 11, 13, 15, 17, and 19 km (Figure 7). The results of the two slip models show that as the depth of the initial rupture point increases, the simulation results of the ground motion parameters also increase. However, the effect of the change in the depth of the initial rupture point on the simulation results was not significant.
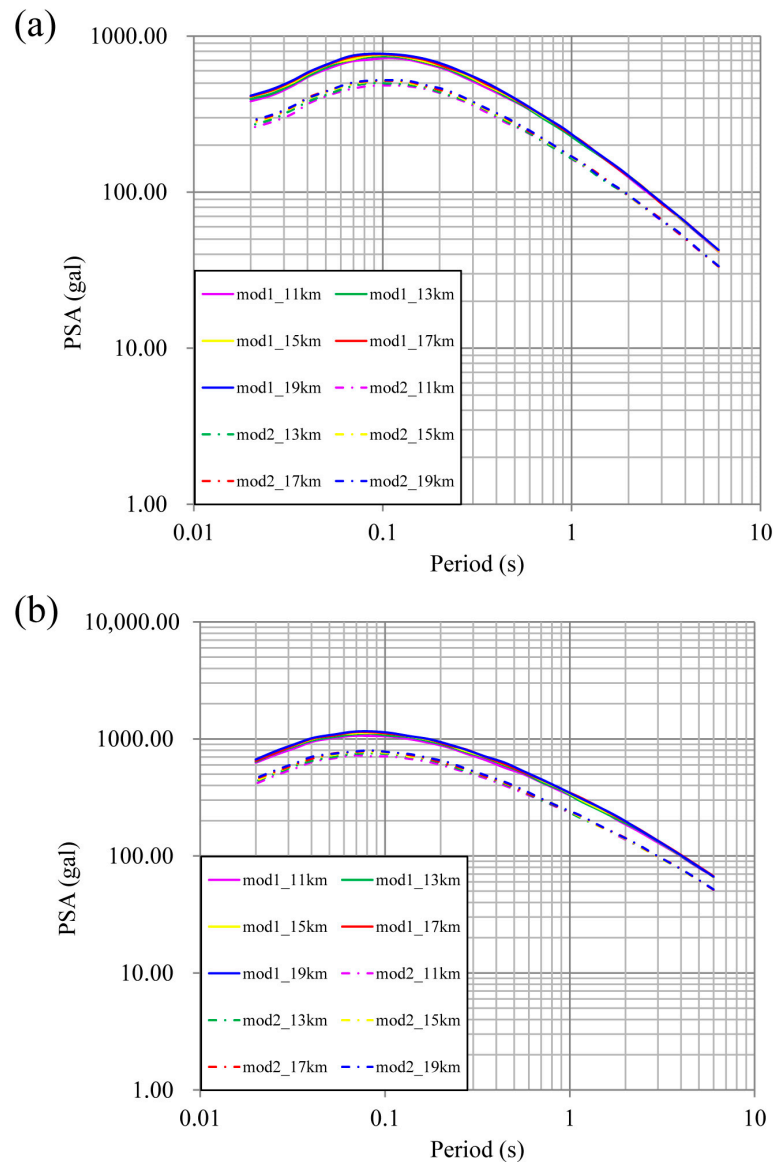
Figure 7. (**a**) The average and (**b**) 84th-percentile acceleration response spectra for different initial rupture point depths.

3.3. The Influence of Sites

We then analyzed and compared the uncertainties of the different site locations based on the results of the multi-scheme ground motion simulations. We used the values and weights of the various simulation parameters (Figure 5), weight scheme 12 (Table 4), and the six different site locations (Figure 1b). The obtained average acceleration response spectra of Slip Models 1 and 2 are shown in Figure 8a,b, respectively. The 84th-percentile results are shown in Figure 8c,d. For Slip Model 1, the average and 84th-percentile acceleration response spectra of Site 1 and Site 2 are higher than those of Site 3, while the results for Sites 4 and 5 are higher than those for Site 6 (Figure 8a,c). Moreover, for both the average and 84th-percentile results, the simulated acceleration response spectra of Site 1, Site 2, and Site 3 are higher than those of Site 4, Site 5, and Site 6, respectively. The results show that when the site is located on the hanging wall of the fault, the acceleration response spectrum is higher than that for a site located on the footwall. We can obtain the same conclusion for Slip Model 2 (Figure 8b,d).
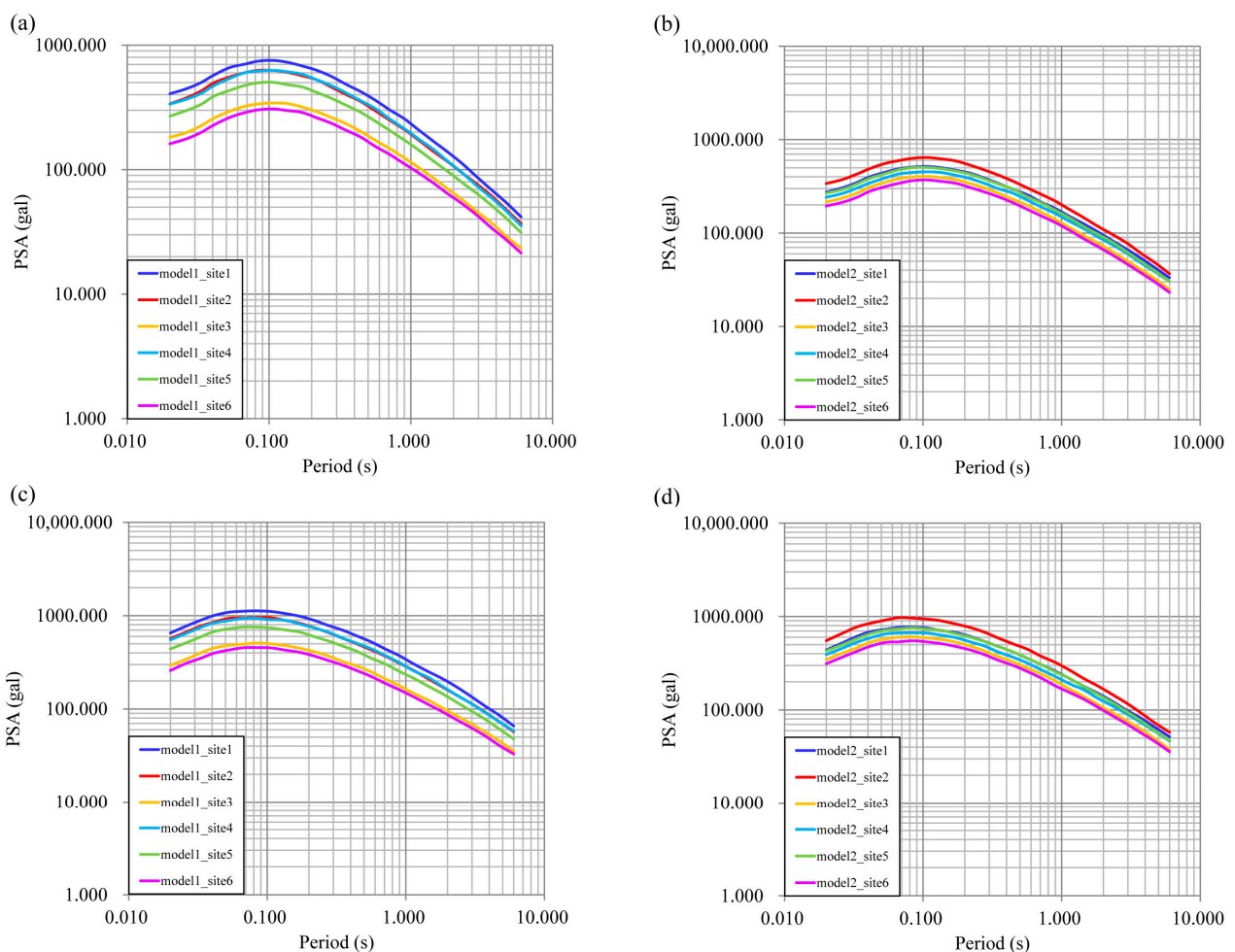
Figure 8. Simulation results for Slip Models 1 and 2 at different sites. The average acceleration response spectra for (**a**) Slip Model 1 and (**b**) Slip Model 2; the 84th-percentile results for (**c**) Slip Model 1 and (**d**) Slip Model 2.

To analyze the reasons for this phenomenon and determine the roles of the different initial rupture points in the results of the ground motion simulations, we further compared the effects of different combinations of sites and initial rupture points on the simulation results yielded by the two source models. We used the same simulation parameters (Figure 5) and Sites 1–3. The average and 84th-percentile values for Slip Model 1 are shown in Figure 9a,b, respectively. For Slip Model 2, the average value is shown in Figure 9c, and

the 84th-percentile result is shown in Figure 9d. As shown in Figure 9, we found that point 1 for the different sites is higher than the other points for the same site in Slip Model 1, and points 2 and 3 are higher than points 1 and 4 in Slip Model 2 at the same site. For the different sites, when the initial rupture point is located near a smaller asperity rather than a larger asperity, the simulation results are greater than those for the other schemes. For both source models, the simulation results for Site 3 are lower than those of Sites 1 and 2. The acceleration response spectra of the four initial rupture points for Site 3 in Slip Model 1 are approximately coincident. However, the result for point 4 is significantly lower than the other three initial rupture points for Slip Model 2, which may be due to the longer distance from the largest asperity to point 4.
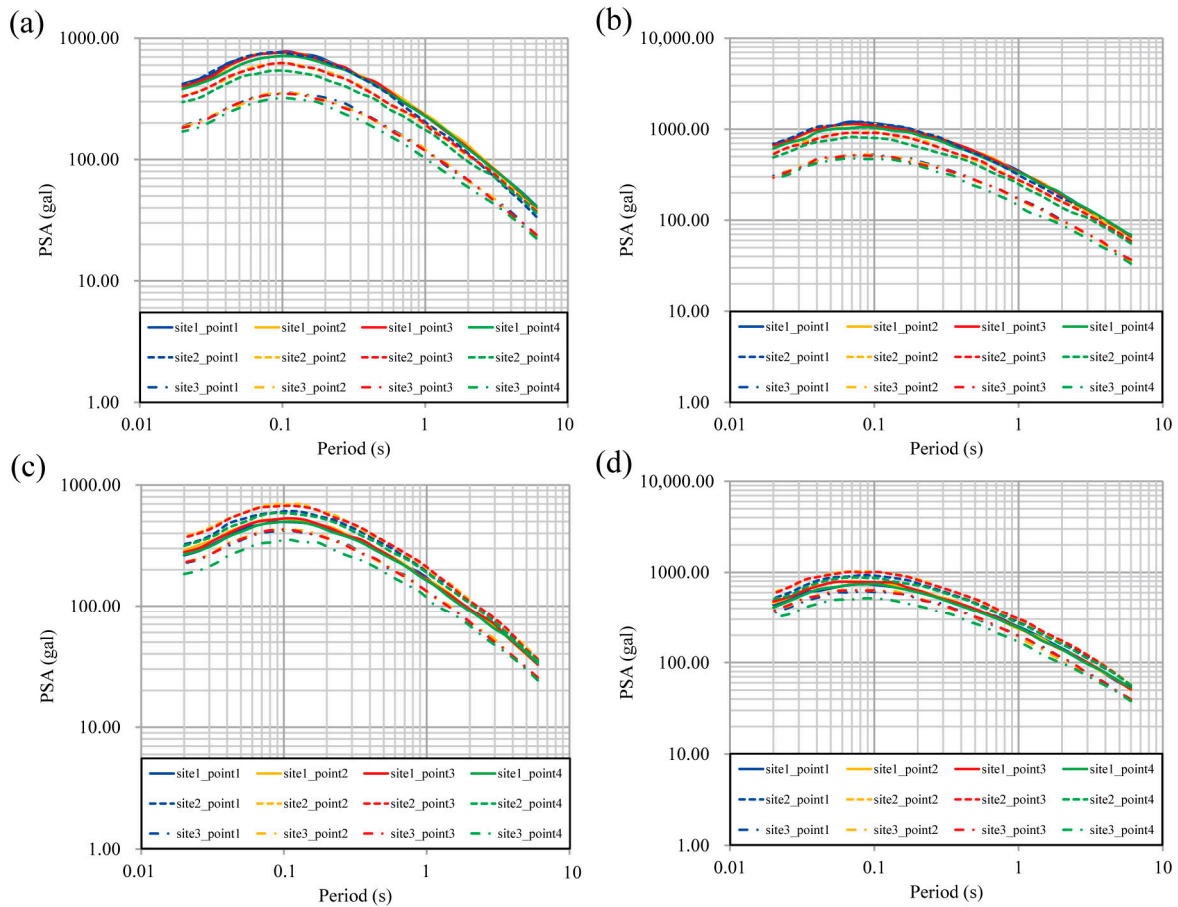
Figure 9. Simulation results with different sites and different initial rupture points for Slip Models 1 and 2. (**a**) The average and (**b**) 84th-percentile values for Slip Model 1; (**c**) the average and (**d**) 84th-percentile values for Slip Model 2.

4. Discussion and Conclusions

To estimate reliable ground motion predictions for an area with sparse seismic data, we considered the effect of parameter uncertainty by calculating different values for the same simulation parameters using the proven stochastic finite-fault method to simulate the near-field strong ground motion of large earthquakes. In this work, our goal was to consider the extreme situation wherein the maximum credible earthquake occurs on the Kalawenguquan fault. Though we obtained the minimum, average, maximum, and 50th-, 84th-, and 95th-percentile PGA values and acceleration response spectra for multi-scheme ground motion simulations, we mainly drew conclusions based on the average and 84th-percentile results. It is worth noting that the 84th-percentile provides the uncertainty of the multi-scheme results calculated using different ground motion simulation parameters and represents the maximum credible ground motion parameters for deterministic seismic hazard.

We analyzed the slip distribution characteristics of Slip Model 1, Slip Model 2, and a random model. We found that when the largest asperity was closer to Site 1 when using Slip Model 2, the minimum, average, maximum, and 50th-, 84th-, and 95th-percentile PGA values were all lower than those of Slip Model 1, wherein the largest asperity was further from the site. The average and 84th-precentile acceleration response spectra for Slip Model 1 are higher than those of Slip Model 2 (Figure 6). This contradicts the notion that higher ground motion parameters are obtained when the largest asperity is located closest to the site. Moreover, it is not suitable to use random models when conducting near-field ground motion simulations for Site 1 for large earthquakes, as they do not represent the maximum ground motion scenario. Though different percentiles of PGA and acceleration response spectra for Slip Model 2 are lower, we think that the geological and geomorphological data have effects on the near-field ground motion simulation. If the location of the largest asperity inferred from the geological and geomorphological data is consistent with that shown in Slip Model 1, its impact on ground motion simulation is significant.

As the weight schemes and depths of the initial rupture point changed, the simulation results showed very little variation. The historical seismic depth, locking depth, and depth distribution of small earthquakes can be used to determine the depth of the initial rupture point. We could also appropriately reduce the value scheme for the initial rupture point in our simulations.

We compared ground motion simulations at different site locations near the F1-3 segment of the Kalawenguquan fault, as shown in Figure 8. The results showed that the response spectra of the sites located on the hanging wall of the fault were higher than those of sites located on the footwall. In Figure 8a–d, as Site 1, Site 2, Site 4, and Site 5 are closer to the largest and other asperities, we found that the results of the ground motion simulations wherein the site was located near the asperities were greater than when the site was located further away from the asperities. In addition, the response spectra of Site 1 are higher than those of Site 2 for Slip Model 1, while the results of Slip Model 2 are the opposite (Figure 8c,d). This indicates that when the site is located on a smaller asperity and has a certain distance from the largest asperity, the simulation results are greater. Nakamura et al. [65] investigated the source rupture process of the 12 May 2008 Wenchuan earthquake. Their results showed that five asperities may have been located along the rupture area, and the initial rupture point was near the second-largest asperity. Fu and Li [23] compared the observed PGA and simulated PGA distributions of 1671 accelerograms from the mainshocks and aftershocks of the Wenchuan M_S 8.0 earthquake recorded at 50 strong-motion observational stations. They found that the observed PGAs of the MZQ station located near the second-largest asperity of the Longmen Shan fault were larger than those for the SFB station, which was near the largest asperity. This result indicates that our conclusion is consistent with an actual strong earthquake.

In Figure 9a,b, we can see that Site 1 and Site 2 at point 1 for Slip Model 1 are relatively close, constituting the highest results of all the schemes. However, for Slip Model 2, the results for Site 1 at different points are lower than those of Site 2. Although the depth of the initial rupture point had limited impact on the ground motion parameters, the relationship between its location on the rupture plane and the distribution of the asperities and site locations had a significant impact on the results. Therefore, this relationship requires careful consideration in near-field ground motion simulations for large earthquakes. How to reasonably determine a source model and whether to choose a random source model need to be considered when simulating the ground motion parameters for near-field strong ground motion at major infrastructure sites.

As mentioned in Section 2, we have provided a detailed description for the selection of ground motion modeling parameters, including the maximum credible earthquake, fault length, fault width, fault dip angle, inclination, high-frequency attenuation (κ_0), quality factor ($Q(f)$), site amplification factor, etc. We fixed other parameters and considered the uncertainty of the dip angle, stress drop, kappa, and initial rupture point in our multi-scheme ground motion simulation. We did not consider the uncertainty of other

parameters, which does not mean that these parameters are not important. On the contrary, the determination of these parameters determines whether the evaluation of ground motion parameters is reasonable, so we described the selection of each parameter earlier.

Yu et al. [19] and Zhang et al. [20] used the stochastic finite-fault method to analyze the effect of the uncertainty of fault dip angle, stress drop, and kappa. The results presented in [19] showed that the PGA values increased with the increase in stress drop and the decrease in kappa. Zhang et al. [20] found that the closer the dip angle is to 90°, the larger the rupture distance and the higher the simulated results obtained. So, we did not discuss these parameters' uncertainties in the results and instead focused on the effect of the initial rupture point, site location, source model, and their weights on the simulation results. Of course, multi-scheme ground motion simulations can also consider the uncertainty of other modeling parameters, such as fault length and fault width. However, as these parameters change, the maximum credible earthquake magnitude and slip model will also change, making the calculations more complex. This issue poses challenges for multi-scheme ground motion simulation, so we need to conduct further research on this aspect.

Our motivation was mainly related to major infrastructure. However, a reliable estimation of ground motion input is also important for common structures belonging to the building stock. We usually use seismic hazard maps to guide the seismic hazard assessment of common structures in China. Since the multi-scheme method is not only applicable to major infrastructure but also to common structures, we can extend the applications of the multi-scheme method in seismic hazard assessment to more engineering structures.

Author Contributions: Conceptualization, J.L. and B.Z.; Funding acquisition, J.L.; Investigation, Z.H., H.J. and L.W.; Methodology, J.L.; Resources, J.L.; Software, J.L.; Supervision, B.Z.; Visualization, J.L. and G.B.; Writing—original draft, J.L.; Writing—review & editing, J.L. All authors have read and agreed to the published version of the manuscript.

Institutional Review Board Statement: Not applicable.

Informed Consent Statement: Not applicable.

Data Availability Statement: The data presented in this study are available on request from the corresponding author.

Conflicts of Interest: The authors declare no conflicts of interest.

References

1. Kang, J.M.; Wang, Z.H.; Cheng, H.B.; Wang, J.; Liu, X.L. Remote sensing land use evolution in earthquake-stricken regions of Wenchuan county, China. *Sustainability* **2022**, *14*, 9721. [CrossRef]
2. Shareef, S.S. Earthquake consideration in architectural design: Guidelines for architects. *Sustainability* **2023**, *15*, 13760. [CrossRef]
3. *EN 1998-1-2:2019.2*; Design of Structures for Earthquake Resistance—Part 1: General Rules, Seismic Actions and Rules for Buildings. European Committee for Standardization: Brussels, Belgium, 2019.
4. International Code Council (ICC). *2018 International Building Code*; International Code Council (ICC): Nappanee, IN, USA, 2017.
5. *GB50011-2010*; Code for Seismic Design of Buildings. China Building Industry Press: Beijing, China, 2010.
6. American Society of Civil Engineers. *Minimum Design Loads for Buildings and Other Structures*; ASCE: Reston, VI, USA, 2010.
7. Yu, Y.X.; Li, S.Y.; Xiao, L. Development of ground motion attenuation relations for the new seismic hazard map of China. *Technol. Earthq. Disast. Prev.* **2013**, *8*, 24–33.
8. Abrahamson, N.A.; Silva, W.J.; Kamai, R. Summary of the ASK14 ground motion relation for active crustal regions. *Earthq. Spectra* **2014**, *30*, 1025–1055. [CrossRef]
9. Boore, D.M.; Stewart, J.P.; Seyhan, E.; Atkinson, G.M. NGA-West2 equations for predicting PGA, PGV, and 5% damped PSA for shallow crustal earthquake. *Earthq. Spectra* **2014**, *30*, 1057–1085. [CrossRef]
10. Campbell, K.W.; Bozorgnia, Y. Average horizontal components of PGA, PGV, and 5% damped linear acceleration response spectra. *Earthq. Spectra* **2014**, *30*, 1087–1115. [CrossRef]

11. Chiou, B.S.J.; Youngs, R.R. Update of the Chiou and Youngs NGA model for the average horizontal component of peak ground motion and response spectra. *Earthq. Spectra* **2014**, *30*, 1117–1153. [CrossRef]
12. Idriss, I.M. An NGA-West2 empirical model for estimating the horizontal spectral values generated by shallow crustal earthquakes. *Earthq. Spectra* **2014**, *30*, 1155–1177. [CrossRef]
13. Iervolino, I.; Manfredi, G.; Cosenza, E. Ground motion duration effects on nonlinear seismic response. *Earthq. Engng. Struct. Dyn.* **2006**, *35*, 21–38. [CrossRef]
14. Barbagallo, F.; Bosco, M.; Ghersi, A.; Marino, E.M.; Rossi, P.P. Seismic assessment of steel MRFs by cyclic pushover analysis. *Open Constr. Build. Technol. J.* **2019**, *13*, 12–26. [CrossRef]
15. Avik, S.; Pranjul, P. Effects of ground motion modification methods and ground motion duration on seismic performance of a 15-storied building. *J. Build. Eng.* **2018**, *15*, 14–25.
16. Oh-Sung, K.; Amr, E. The effect of material and ground motion uncertainty on the seismic vulnerability curves of RC structure. *Eng. Struct.* **2006**, *28*, 289–303.
17. Fu, L.; Li, X.J.; Wang, F.; Chen, S. A study of site response and regional attenuation in the Longmen Shan region, eastern Tibetan Plateau, SW China, from seismic recordings using the generalized inversion method. *J. Asian Earth Sci.* **2019**, *181*, 103887. [CrossRef]
18. Xia, C.; Zhao, B.M.; Horike, M.; Kagawa, T. Strong ground motion simulations of the M_W 7.9 Wenchuan earthquake using the empirical green's function method. *Bull. Seismol. Soc. Am.* **2015**, *105*, 1383–1397. [CrossRef]
19. Yu, R.F.; Shi, H.T.; Sun, J.Z.; Zhang, D.F.; Yu, Y.X. Comprehensive evaluation of ground motion parameters for dam site based on stochastic finite fault method. *China Civ. Eng. J.* **2020**, *53*, 314–328.
20. Zhang, D.F.; Fu, C.H.; Lv, H.S.; Yu, R.F. Stochastic finite fault method and its engineering applications. *Technol. Earthq. Disast. Prev.* **2018**, *13*, 784–800.
21. Atkinson, G.M.; Goda, K.; Assatourians, K. Comparison of nonlinear structural responses for accelerograms simulated from the stochastic finite-fault approach versus the hybrid broadband approach. *Bull. Seismol. Soc. Am.* **2011**, *101*, 2967–2980. [CrossRef]
22. Beresnev, I.A.; Atkinson, G.M. FINSIM-A FORTRAN program for simulating stochastic acceleration time histories from finite faults. *Seismol. Res. Lett.* **1998**, *69*, 27–32. [CrossRef]
23. Fu, L.; Li, X.J. The kappa (κ_0) model of the Longmenshan region and its application to simulation of strong ground-motion by the Wenchuan M_S 8.0 earthquake. *Chin. J. Geophys.* **2017**, *60*, 2935–2947. [CrossRef]
24. Hartzell, S.H. Earthquake aftershock as Green's functions. *Geophys. Res. Lett.* **1978**, *5*, 1–4. [CrossRef]
25. Irikura, K. Semi-empirical estimation of strong ground motions during large earthquake. *Bull. Disaster Prev. Res. Inst.* **1983**, *33*, 63–104.
26. Sun, J.Z.; Yu, Y.X.; Li, Y.Q. Stochastic finite-fault simulation of the 2017 Jiuzhaigou earthquake in China. *Earth Planets Space* **2018**, *70*, 128. [CrossRef]
27. Wang, H.Y. Prediction of acceleration field of the 14 April 2010 Yushu earthquake. *Chin. J. Geophys.* **2010**, *53*, 2345–2354. [CrossRef]
28. Zhang, C.R.; Chen, H.Q.; Li, M. Generation of the maximum credible earthquake by using the stochastic finite fault method. *J. Hydraul. Eng.* **2011**, *42*, 721–728.
29. Zhou, H.; Chang, Y. Stochastic finite-fault method controlled by the fault rupture process and its application to the M_S 7.0 Lushan earthquake. *Soil Dyn. Earthq. Eng.* **2019**, *126*, 105782. [CrossRef]
30. Boore, D.M. Stochastic simulation of high-frequency ground motions based on seismological models of the radiated spectra. *Bull. Seismol. Soc. Am.* **1983**, *73*, 1865–1894.
31. Molnar, P.; Tapponnier, P. Cenozoic tectonics of Asia: Effects of a continental collision: Features of recent continental tectonics in Asia can be interpreted as results of the India-Eurasia collision. *Science* **1975**, *189*, 419–426. [CrossRef]
32. Tapponnier, P.; Molnar, P. Active faulting and Cenozoic tectonics of the Tien Shan, Mongolia, and Baykal Regions. *J. Geophys. Res. Solid Earth* **1979**, *84*, 3425–3459. [CrossRef]
33. Avouac, J.P.; Tapponnier, P.; Bai, M.; You, H.; Wang, G. Active thrusting and folding along the northern Tien Shan and Late Cenozoic rotation of the Tarim relative to Dzungaria and Kazakhstan. *J. Geophys. Res. Solid Earth* **1993**, *98*, 6755–6804. [CrossRef]
34. Burchfiel, B.C.; Brown, E.T.; Deng, Q.D.; Feng, X.Y.; Li, J.; Molnar, P.; Shi, J.B.; Wu, Z.M.; You, H.C. Crustal shortening on the margins of the Tien Shan, Xinjiang, China. *Int. Geol. Rev.* **1999**, *41*, 665–700. [CrossRef]
35. Deng, Q.D.; Feng, X.Y.; Zhang, P.Z.; Xu, X.W.; Yang, X.P.; Peng, S.Z.; Li, J. *Active Tectonics of the Chinese Tianshan Mountain*; Seismological Press: Beijing, China, 2000.
36. Wang, M.; Shen, Z.K. Present-day crustal deformation of continental China derived from GPS and its tectonic implications. *J. Geophys. Res. Solid Earth* **2020**, *125*, e2019JB018774. [CrossRef]
37. Chen, F.Q. Remote sensing interpretation and analysis of key engineering geological problems in the Nalati Mountain crossing section of the Yining-Aksu Railway. *Bull. Geol. Sci. Technol.* **2023**, *42*, 288–296.
38. Charreau, J.; Saint-Carlier, D.; Dominguez, S.; Lavé, J.; Blard, P.H.; Avouac, J.P.; Jolivet, M.; Chen, Y.; Wang, S.L.; Brown, N.D.; et al. Denudation outpaced by crustal thickening in the eastern Tianshan. *Earth Planet. Sci. Lett.* **2017**, *479*, 179–191. [CrossRef]
39. Wu, C.Y.; Wu, G.D.; Chen, J.B.; Alimujiang, Y.; Chang, X.D.; Li, S. The late-quaternary activity rate of Nalati fault, interior Tianshan. *Inland Earthq.* **2013**, *27*, 97–105.
40. Wang, L.; Ren, Z.K.; He, Z.T.; Ji, H.M.; Liu, J.R.; Guo, L.; Li, X.A. Holocene activity eviden of the Nalati fault zone within the Tianshan. *Seismol. Geol.* **2024**, *in press*.

41. Li, Y.Z.; Nie, X.H.; Xia, A.G.; Gao, G. A summary of Tekesi M_S 5.9 earthquake occurred on July 20, 2007 and some seismological precursory anomalies. *Earthq. Res. China* **2008**, *24*, 370–378.

42. Wells, D.L.; Coppersmith, K.J. New empirical relationships among magnitude, rupture length, rupture width, rupture area, and surface displacement. *Bull. Seismol. Soc. Am.* **1994**, *84*, 974–1002. [CrossRef]

43. Cheng, J.; Rong, Y.F.; Magistrale, H.; Chen, G.H.; Xu, X.W. An M_W-Based historical earthquake catalog for Mainland China. *Bull Seismol. Soc. Am.* **2017**, *107*, 2490–2500. [CrossRef]

44. Tang, L.L.; Li, Z.H. Ground motion attenuation, site response and source parameters of earthquakes in middle and eastern range of Tianshan mountain, Xinjiang of China. *Acta Seismol. Sin.* **2011**, *33*, 134–142.

45. Atkinson, G.M.; Mereu, R.F. The shape of ground motion attenuation curves in southeastern Canada. *Bull Seismol. Soc. Am.* **1992**, *8*, 2014–2031. [CrossRef]

46. Liu, J.M.; Li, Z.H. Non-elastic attenuation, site response and source parameters in the northern Tianshan Mountain, Xinjiang of China. *Earthquake* **2014**, *34*, 77–86.

47. Zhao, C.P.; Chen, Z.L.; Hua, W.; Wang, Q.C.; Li, Z.X.; Zheng, S.H. Study on source parameters of small to moderate earthquakes in the main seismic active regions, China mainland. *Chin. J. Geophys.* **2011**, *54*, 1478–1489.

48. Xia, A.G. Preliminary study on stress drop variation characteristic of Yutian M_S7.3 earthquake on Feb.12, 2014, Xinjiang. *Inland Earthq.* **2014**, *28*, 138–141.

49. Atkinson, G.M.; Silva, W. An empirical study of earthquake source spectra for California earthquakes. *Bull. Seismol. Soc. Am.* **1997**, *87*, 97–113. [CrossRef]

50. Campbell, K.W. Estimates of shear-Wave Q and κ_0 for unconsolidated and semiconsolidated sediments in eastern North America. *Bull. Seismol. Soc. Am.* **2009**, *99*, 2365–2392. [CrossRef]

51. Fu, L.; Li, X.J. The characteristics of high-frequency attenuation of shear waves in the Longmen Shan and adjacent regions. *Bull. Seismol. Soc. Am.* **2016**, *106*, 1979–1990. [CrossRef]

52. Fu, L.; Chen, S.; Li, J.Y.; Zhang, L.B.; Xie, J.J.; Li, X.J. Regional spectral characteristics derived using the generalized inversion technique and applications to stochastic simulation of the 2021 M_W 6.1 Yangbi earthquake. *Bull. Seismol. Soc. Am.* **2023**, *113*, 378–400. [CrossRef]

53. Liu, J.M.; Wu, C.Y.; Yu, H.Z.; Wang, Q.; Liu, D.Q.; Zhao, B.B.; Gao, R.; Gao, G.; Kong, X.Y. P-wave velocity structure of the crust and uppermost mantle in the middle of Tianshan. *Chin. J. Gepphys.* **2023**, *66*, 1348–1362.

54. Joyner, W.B.; Boore, D.M. On simulating large earthquakes by Green's-Function addition of smaller earthquakes. *Earthq. Source Mech.* **1986**, *37*, 269–274.

55. Somerville, P.; Irikura, K.; Graves, R.; Sawada, S.; Wald, D.; Abrahamson, N.; Iwasaki, Y.; Smith, N.; Kowada, A. Characterizing crustal earthquake slip models for the prediction of strong ground motion. *Seismol. Res. Lett.* **1999**, *70*, 59–80. [CrossRef]

56. Stein, R.S. Appendix D: Earthquake Rate Model 2 of the 2007 Working Group for California Earthquake Probabilities, Magnitude-Area Relationships. *US Geol. Surv. Open File Rep.* **2008**, 1–16.

57. Hanks, T.C.; Kanamori, H. A moment magnitude scale. *J. Geophys. Res.* **1979**, *84*, 2348–2350. [CrossRef]

58. Wang, H.Y. Finite Fault Source Model for Predicting Near-Field Strong Ground Motion. Ph.D. Thesis, Institute of Engineering Mechanics, China Earthquake Administration, Harbin, China, 2004.

59. Wang, S.; Gao, G. Regional characteristics of modern tectonic stress field in Xinjiang and its adjacent areas. *Acta Seismol. Sin.* **1992**, *14*, 612–620.

60. Motazedian, D.; Atkinson, G.M. Stochastic finite-fault modeling based on a dynamic corner frequency. *Bull. Seismol. Soc. Am.* **2005**, *95*, 995–1010. [CrossRef]

61. Boore, D.M. Short-period P- and S-wave radiation from large earthquakes: Implications for spectral scaling relations. *Bull. Seismol. Soc. Am.* **1986**, *76*, 43–64.

62. Boore, D.M. Simulation of ground motion using the stochastic method. *Pure Appl. Geophys.* **2003**, *160*, 635–676. [CrossRef]

63. Anderson, J.G.; Hough, S.E. A model for the shape of the Fourier amplitude spectrum of acceleration at high frequency. *Bull. Seismol. Soc. Am.* **1984**, *74*, 1969–1993.

64. Boore, D.M. Comparing stochastic point-source and finite-source ground-motion simulation: SMSIM and EXSIM. *Bull. Seismol. Soc. Am.* **2009**, *99*, 3202–3216. [CrossRef]

65. Nakamura, T.; Tsuboi, S.; Kaneda, Y.; Yamanaka, Y. Rupture process of the 2008 Wenchuan, China earthquake inferred from teleseismic waveform inversion and forward modeling of broadband seismic waves. *Tectomophysics* **2010**, *491*, 7284. [CrossRef]